Electromagnetic Scattering by an Arbitrarily Shaped Surface with an Anisotropic Impedance Boundary Condition

Allen W. Glisson
Department of Electrical Engineering
University of Mississippi
University, MS 38677

Mark Orman, Frank Falco, and Donald Koppel
Riverside Research Institute
330 West 42nd St.
New York, NY 10036

Abstract *- The problem of electromagnetic scattering from arbitrarily shaped, imperfectly conducting surfaces that can be represented by an anisotropic impedance boundary condition is solved numerically using the electric field integral equation and a triangular patch model for the surface. The anisotropic impedance boundary condition function is described by a constant surface dyadic within each triangular face. The procedure is validated by comparison of numerical results obtained with the triangular patch model with body of revolution model results for problems involving scattering by spheres and cylinders having uniform or anisotropic impedance boundary conditions.*

I. Introduction

Many problems of interest in electromagnetic scattering involve imperfectly conducting bodies. The impedance boundary condition (IBC) [1] is often used to modeling specific classes of such bodies in electromagnetic scattering problems. The IBC is an approximate boundary condition that relates the tangential electric and magnetic fields at the body surface via an impedance parameter, which is a dyadic in the case of an anisotropic surface impedance. When the approximation is valid, it can be used effectively to reduce the number of unknowns required in the numerical solution process by a factor of two. Senior has examined the conditions for which the IBC is valid [2], and Mitzner has presented a surface integral equation formulation for scattering by bodies that are represented by an IBC [3]. The impedance relationship is often obtained through the solution of a canonical problem, such as scattering of a plane wave from an imperfectly conducting ground plane having the constitutive parameters of the scatterer of interest, and the relationship is then assumed to apply locally to the nonplanar surface of the scatterer. The IBC represents a good approximation in such cases if the magnitude of the complex refractive index of the scatterer material is much greater than unity and if the radius of curvature of the scatterer is sufficiently large. The impedance boundary condition has been used to model high-conductivity scatterers, absorbing coatings, plasma coatings, corrugated surfaces, rough surfaces, and other configurations [4-8]. The applicability of various types of integral equations in modeling IBC problems has been studied by various investigators [9-14]. Numerical solutions for scattering by arbitrarily shaped bodies having isotropic IBC's have been presented using a pulse expansion, point matching procedure by Sebak and Shafai [15] and using the triangular patch modeling method by Glisson [16]. The use of more accurate generalized impedance boundary conditions in the numerical solution of two-dimensional electromagnetic scattering problems has also been demonstrated [17] and higher order IBC's applied to bodies of revolution have been presented [18]. Anisotropic surface impedances have been employed in frequency selective surfaces by Orta *et al* [19]. Numerical solutions for bodies of revolution with anisotropic IBC's have been presented in [20], and a comparison of different integral equation formulations for bodies of revolution with anisotropic IBC's has been presented in [21].

In this work the solution of electromagnetic scattering problems involving an arbitrarily shaped body with an anisotropic impedance boundary condition is formulated and implemented. The triangular patch model described by Rao *et al* [22] serves as the basis for the development. The triangular patch code originally employed the electric field integral equation (EFIE) formulation and was applicable only to scattering problems involving perfectly conducting

bodies, which could be either closed bodies or thin open surfaces. In this work the anisotropic IBC model is included in the EFIE to represent an approximate model for specific classes of imperfectly conducting closed bodies. The implementation permits modeling of objects that are relatively thin in terms of wavelength [23]. Results are validated by comparison of patch code results with results obtained with a body of revolution solution procedure. The formulation of the surface integral equation is presented briefly in Section II, and the numerical implementation is described in Section III. Numerical results are given in Section IV.

II. Integral Equation Formulation

The electric field integral equation for a body having an impedance boundary condition can be developed from the equivalence principle [24] by first removing the scatterer from the medium in which it resides and placing equivalent electric and magnetic surface currents $\mathbf{J}$ and $\mathbf{M}$ along the surface forming the boundary of the scatterer in the original problem. The equivalent currents radiate in an infinite homogeneous region and are defined by the relations $\mathbf{J}=\hat{\mathbf{n}}\times\mathbf{H}$ and $\mathbf{M}=\mathbf{E}\times\hat{\mathbf{n}}$, where $\mathbf{E}$ and $\mathbf{H}$ are the total electric and magnetic fields at the surface of the scatterer in the original problem. With the equivalent currents defined in this manner, they will radiate the correct scattered field for the original problem in the region exterior to the scatterer, and will radiate the negative of the incident field in the region interior to the scatterer surface. The EFIE for the impedance body can therefore be written as

$$-\hat{\mathbf{n}}\times\hat{\mathbf{n}}\times\mathbf{E}^i=\hat{\mathbf{n}}\times\hat{\mathbf{n}}\times\mathbf{E}^s \quad , \quad \mathbf{r}\to S^- \tag{1}$$

where $\mathbf{E}^i$ is the incident electric field, $\mathbf{E}^s$ is the scattered electric field, and $\hat{\mathbf{n}}$ is the outward directed unit normal at the surface of the scatterer. Eq. (1) is valid in the limit as the observation point $\mathbf{r}$ approaches the surface from the interior, denoted by S^-. A similar equation valid in the limit as $\mathbf{r}$ approaches the surface from the exterior may be obtained from the definition of the equivalent magnetic current. The equation which results after the limit operations are performed is the same in both cases.

The scattered electric field $\mathbf{E}^s$ may be represented in terms of potential functions as

$$\mathbf{E}^s(\mathbf{r}) = -j\omega\mathbf{A}(\mathbf{r}) - \nabla\Phi(\mathbf{r}) - \frac{1}{\epsilon}\nabla\times\mathbf{F}(\mathbf{r}) \tag{2}$$

where

$$\mathbf{A}(\mathbf{r}) = \mu\int_S \mathbf{J}(\mathbf{r}')G(\mathbf{r},\mathbf{r}')dS' \tag{3a}$$

$$\Phi(\mathbf{r}) = \frac{1}{\epsilon}\int_S \sigma(\mathbf{r}')G(\mathbf{r},\mathbf{r}')dS' \tag{3b}$$

$$\mathbf{F}(\mathbf{r}) = \epsilon\int_S \mathbf{M}(\mathbf{r}')G(\mathbf{r},\mathbf{r}')dS' \tag{3c}$$

and where

$$G(\mathbf{r},\mathbf{r}') = \frac{e^{-jk|\mathbf{r}-\mathbf{r}'|}}{4\pi|\mathbf{r}-\mathbf{r}'|} \tag{4}$$

In (3) and (4) $\mathbf{r}$ and $\mathbf{r}'$ represent the observation and source coordinates, respectively, ϵ, μ, and k are the permittivity, permeability, and the wavenumber of the exterior region, respectively, and σ is the equivalent electric surface charge density, which is related to $\mathbf{J}$ through the continuity equation. A harmonic time variation $\exp(j\omega t)$ is assumed and suppressed.

The scattered electric field given by (2) is evaluated in the limit as $\mathbf{r}$ approaches the scatterer surface from the interior. The scattered field expression resulting from the limit process is valid just inside the scatterer surface, and it may be substituted into (1) to represent the boundary condition just inside the scatterer surface as an integral equation in the unknown surface currents $\mathbf{J}$ and $\mathbf{M}$. Additional boundary condition information must be enforced to uniquely determine both equivalent current sets, however. When applicable, the impedance boundary condition, which relates the tangential components of the electric and magnetic fields at the scatterer surface, may be enforced to provide the necessary additional information. The IBC considered in this work is the anisotropic impedance boundary condition, which relates the surface electric and magnetic fields by any one of several equivalent expressions:

$$\begin{aligned} \mathbf{E}-(\mathbf{E}\cdot\hat{\mathbf{n}})\hat{\mathbf{n}} &= \eta\underline{\mathbf{Z}}_s\cdot(\hat{\mathbf{n}}\times\mathbf{H}) \\ -\hat{\mathbf{n}}\times\hat{\mathbf{n}}\times\mathbf{E} &= \eta\underline{\mathbf{Z}}_s\cdot(\hat{\mathbf{n}}\times\mathbf{H}) \\ \hat{\mathbf{n}}\times\mathbf{E} &= \eta\hat{\mathbf{n}}\times[\underline{\mathbf{Z}}_s\cdot(\hat{\mathbf{n}}\times\mathbf{H})] \end{aligned} \tag{5}$$

where the anisotropic IBC surface impedance dyadic is normalized by the intrinsic impedance of free space η and is defined by

$$\begin{aligned} \underline{\mathbf{Z}}_s &= Z_{11}\hat{\mathbf{a}}_1\hat{\mathbf{a}}_1 + Z_{12}\hat{\mathbf{a}}_1\hat{\mathbf{a}}_2 + Z_{21}\hat{\mathbf{a}}_2\hat{\mathbf{a}}_1 + Z_{22}\hat{\mathbf{a}}_2\hat{\mathbf{a}}_2 \\ &= \begin{bmatrix} Z_{11}\hat{\mathbf{a}}_1\hat{\mathbf{a}}_1 & Z_{12}\hat{\mathbf{a}}_1\hat{\mathbf{a}}_2 \\ Z_{21}\hat{\mathbf{a}}_2\hat{\mathbf{a}}_1 & Z_{22}\hat{\mathbf{a}}_2\hat{\mathbf{a}}_2 \end{bmatrix} \end{aligned} \tag{6}$$

and where $\hat{\mathbf{a}}_1$ and $\hat{\mathbf{a}}_2$ are unit vectors in an orthogonal

coordinate system defined on the surface S. The orientation of these unit vectors is assumed to satisfy $\hat{\mathbf{a}}_2 = \hat{\mathbf{n}} \times \hat{\mathbf{a}}_1$, where $\hat{\mathbf{n}}$ is the outward-directed unit surface normal. In terms of the equivalent electric and magnetic surface currents, the anisotropic IBC may be represented by

$$\mathbf{M} = -\eta \hat{\mathbf{n}} \times [\underline{\mathbf{Z}}_s \cdot \mathbf{J}] \tag{7}$$

Thus, one finally obtains the EFIE for a scatterer with an anisotropic impedance boundary condition:

$$\mathbf{E}^i_{tan}(\mathbf{r}) = [j\omega\mu \int_S \mathbf{J} G(\mathbf{r},\mathbf{r}')dS' + \frac{1}{\epsilon}\nabla \int_S \sigma G(\mathbf{r},\mathbf{r}')dS' - \int_S \eta \{\hat{\mathbf{n}} \times [\underline{\mathbf{Z}}_s \cdot \mathbf{J}]\} \times \nabla G(\mathbf{r},\mathbf{r}')dS']_{tan}, \quad \mathbf{r} \to S^- \tag{8}$$

where $\mathbf{r} \to S^-$ denotes that the equation is valid in the limit as the observation point approaches S from the interior of S. The equivalent electric surface current $\mathbf{J}$ is then the only unknown quantity and (8) may be solved for $\mathbf{J}$ via the method of moments [25].

III. Numerical Solution Procedure

The triangular patch modeling method developed by Rao, Wilton, and Glisson [22] is employed to solve (8) for the unknown electric surface current density $\mathbf{J}$. A suitable triangular patch model of the geometry of the impedance body is first developed. The electric surface current density $\mathbf{J}$ on S is then approximated in terms of basis functions $\mathbf{f}_n$ defined on pairs of triangles as

$$\mathbf{J}(\mathbf{r}) \simeq \sum_{n=1}^{N} I_n \mathbf{f}_n(\mathbf{r}) \tag{9}$$

where N is the number of interior edges in the model. Various geometrical quantities associated with a triangle pair with common edge n are illustrated in Figure 1. The two triangles attached to the common edge are denoted as T_n^+ and T_n^-. Points within triangle T_n^+ may be defined by a position vector $\mathbf{r}$ with respect to a global coordinate origin O, or by a local position vector $\boldsymbol{\rho}_n^+$ defined with respect to the free vertex of T_n^+. Quantities in T_n^- are defined similarly except that the vector $\boldsymbol{\rho}_n^-$ is directed toward the free vertex of T_n^- rather than away from it. The vector basis function $\mathbf{f}_n$ representing the electric surface current density associated with the n^{th} edge is then defined as

$$\mathbf{f}_n(\mathbf{r}) = \begin{cases} \dfrac{\ell_n}{2A_n^+}\boldsymbol{\rho}_n^+, & \mathbf{r} \in T_n^+ \\ \dfrac{\ell_n}{2A_n^-}\boldsymbol{\rho}_n^-, & \mathbf{r} \in T_n^- \\ \mathbf{0}, & \text{otherwise} \end{cases} \tag{10}$$

where ℓ_n is the length of edge n and $A_n^{\pm}$ is the area of triangle $T_n^{\pm}$.

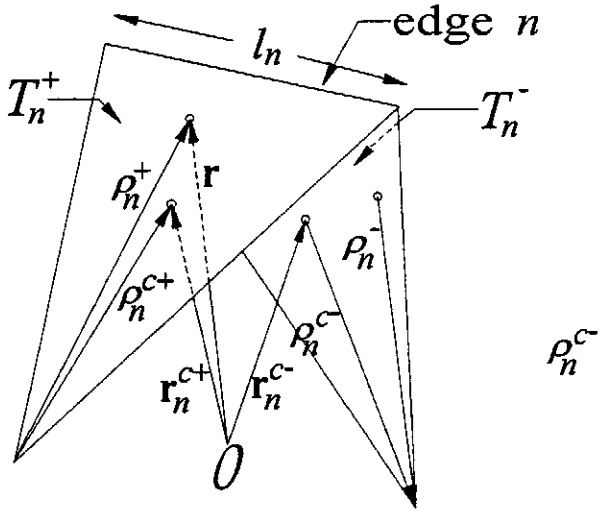

Figure 1. Geometrical parameters associated with a triangle pair.

The method of moments is applied by next testing (8) with suitable testing functions. The testing functions are chosen to be the expansion functions $\mathbf{f}_n$ defined in the preceding paragraph. Thus, (8) is tested with $\mathbf{f}_m$, $m=1,2,\ldots,N$, and the result can be represented as

$$\langle \mathbf{E}^i, \mathbf{f}_m \rangle = j\omega \langle \mathbf{A}, \mathbf{f}_m \rangle + \langle \nabla\Phi, \mathbf{f}_m \rangle + \frac{1}{\epsilon}\langle \nabla \times \mathbf{F}, \mathbf{f}_m \rangle \tag{11}$$

where the symmetric product is defined as

$$\langle \mathbf{f}, \mathbf{g} \rangle \equiv \int_S \mathbf{f} \cdot \mathbf{g}\, dS \tag{12}$$

and where the curl term in (11) is understood to be evaluated in the limit as the observation point approaches the surface from the interior, as indicated in (8). The Galerkin solution procedure implied by (11) when the basis and testing functions are the same has often been approximated in previous triangular patch code implementations. In this work the expressions for the terms in (11) are presented without these approximations. Appropriate approximations may be made to reduce the amount of numerical integration required if desired.

The evaluation of the magnetic vector potential term and the electric scalar potential term as they appear in (11) is discussed in [22]. However, in this work the vector potential is evaluated directly in terms of its vector integrand rather than expressing the result as a sum of scalar integrals times constant vectors as in [22]. This is done to simplify the implementation of the full Galerkin testing procedure, which involves double surface integration. As in previous work, however, integrations are performed on source triangle, observation triangle pairs rather than on source basis function, observation basis function pairs. One then finds that the vector potential integrations are all of the form

$$A_{ij}^{pq} = \mu \int_{T^p} \frac{\ell_i}{2A^p}(\mathbf{r}-\mathbf{r}_i) \cdot \int_{T^q} \frac{\ell_j}{2A^q}(\mathbf{r}'-\mathbf{r}_j) G dS' dS$$

$$= \frac{\mu \ell_i \ell_j}{16\pi A^p A^q} \left\{ \int_{T^p}\int_{T^q} (\mathbf{r}-\mathbf{r}_i)\cdot(\mathbf{r}'-\mathbf{r}_j)\frac{e^{-jkR}-I_s}{R} dS' dS \right.$$

$$\left. + I_s \int_{T^p} (\mathbf{r}-\mathbf{r}_i) \cdot \left[\int_{T^q} (\mathbf{r}'-\mathbf{r}_j)\frac{1}{R} dS' \right] dS \right\}, \quad \mathbf{r}\epsilon T^p, \mathbf{r}'\epsilon T^q \tag{13}$$

where $R = |\mathbf{R}| = |\mathbf{r}-\mathbf{r}'|$, the indices p and q refer to the observation and source face numbers, respectively, and the indices i and j are local indices referring to the three different testing and basis functions, respectively, that exist within the testing and source faces. Then, for example, ℓ_j refers to the length of the edge with local edge number j and is associated with the j^{th} (local) basis function, while the position vector $\mathbf{r}_j$ locates the vertex opposite the edge with local edge number j in face q. The quantity I_s in (13) is a control variable that is set to 1 if extraction of the singular term in the integrand is to be performed, and that is set to 0 if no singularity extraction is to be performed. When the singularity extraction procedure is performed, the integration of the singular term over the source region can be evaluated analytically as

$$\int_{T^q} (\mathbf{r}'-\mathbf{r}_j)\frac{1}{R} dS' = \int_{T^q} \frac{\rho'-\rho}{R} dS' + (\rho-\rho_j)\int_{T^q} \frac{1}{R} dS' \tag{14}$$

$$= \mathbf{b}^q(\mathbf{r}) + (\rho-\rho_j) a^q(\mathbf{r})$$

where the integrals for $\mathbf{b}^q(\mathbf{r})$ and $a^q(\mathbf{r})$ have been evaluated in [26]. The cylindrical coordinate vectors ρ in (14) represent the projections of the corresponding global position vectors $\mathbf{r}$ onto the plane of the source triangle as described in and as indicated in Fig. 2, where a local coordinate system has been illustrated for use in evaluating a variety of integrals [26]. The definitions for $\mathbf{b}^q(\mathbf{r})$ and $a^q(\mathbf{r})$ are repeated here for completeness:

$$a^q(\mathbf{r}) = \sum_j \hat{\mathbf{P}}_j^0 \cdot \hat{\mathbf{u}}_j \left[P_j^0 \ln(G_j) - |d| \left(\tan^{-1}(F_j^+) - \tan^{-1}(F_j^+) \right) \right] \tag{15}$$

$$\mathbf{b}^q(\mathbf{r}) = \frac{1}{2}\sum_j \hat{\mathbf{u}}_j \left[(R_j^0)^2 \ln(G_j) + \ell_j^+ R_j^+ - \ell_j^- R_j^- \right] \tag{16}$$

where

$$G_j = \frac{R_j^+ + \ell_j^+}{R_j^- + \ell_j^-} = \frac{R_j^- - \ell_j^-}{R_j^+ - \ell_j^+} \tag{17}$$

$$F_j^{\pm} = \frac{P_j^0 \ell_j^{\pm}}{(R_j^0)^2 + |d| R_j^{\pm}} \tag{18}$$

The remaining quantities appearing in (15)-(18) are defined as indicated by Fig. 2.

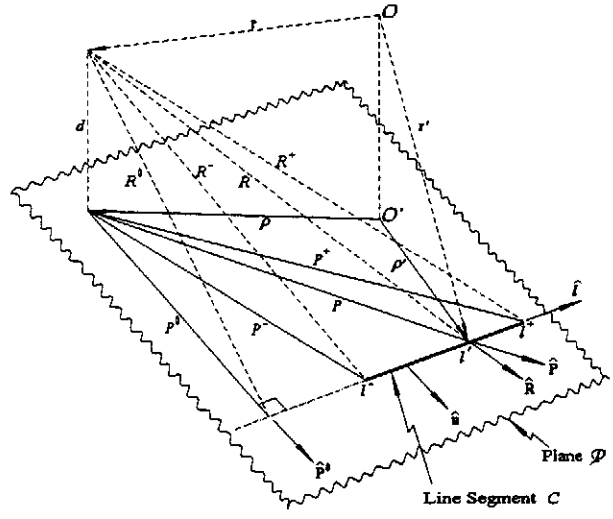

Figure 2. Geometrical quantities associated with the line segment C lying in plane $\mathcal{P}$ and the arbitrary observation point $\mathbf{r}$.

The first step in the evaluation of the scalar potential term in (11) involves the use of a vector calculus identity for surface integration [27] and the particular properties of the basis function or testing function at the edges of its domain of support. The scalar potential term is thus re-expressed as

$$<\nabla\Phi,\mathbf{f}_m> = -\int_S \Phi(\nabla_s\cdot\mathbf{f}_m)dS \qquad (19)$$

When the integration process is performed on a face-by-face basis, the integrals which must be evaluated are of the form

$$\Phi_{ij}^{pq} = \frac{\ell_i\ell_j}{4\pi j\omega\epsilon A^p A^q}\int_{T^p}\int_{T^q}\frac{e^{-jkR}}{R}dS'dS \qquad (20)$$

where, as in the vector potential term, the source region integration can be expressed in terms of bounded and singular integrand portions as

$$\int_{T^q}\frac{e^{-jkR}}{R}dS' = \int_{T^q}\frac{e^{-jkR}-I_s}{R}dS' + I_s\int_{T^q}\frac{1}{R}dS' \qquad (21)$$

The last integral on the right in (21) contains the singular integrand and can be evaluated analytically. The result is simply $a^q(\mathbf{r})$ as given by (15).

The singularity extraction process described above for the magnetic vector potential and the scalar potential terms was performed for all source-face, testing-face combinations in the original implementation of the triangular patch computer code (i.e., I_s was set to 1 for all source-face, testing-face combinations). This seems unnecessary for the general case and it may lead to numerical inaccuracies in matrix element computations when the source face and testing face are far removed from each other and the testing face also lies near the linear extension of one of the edges of the source triangle. The errors appear to result from the evaluation of G_j as given by (17) when the $\ell_j^{\pm}$ tend to cancel the $R_j^{\pm}$ terms. For widely separated source and testing faces, these errors can be eliminated by setting $I_s=0$. Similar errors may also occur for nearby source and testing faces when the subdomain scheme is not completely regular. Therefore, two forms for G_j are given in (17). The first should be used when the $\ell_j^{\pm}$ are both positive, the second when the $\ell_j^{\pm}$ are both negative, and in other cases either expression may be used.

The accurate evaluation of the electric vector potential term in (11) using singularity extraction procedures has been previously addressed for the isotropic case [23, 28]. For this term, if the source face and the testing face are not the same (i.e., for a non-self term) the curl operator may be carried under the source integral and appropriate vector identities may be applied. Thus, the integration required for a source face q and an observation face p becomes

$$\left[\frac{1}{\epsilon}<\nabla\times\mathbf{F}(\mathbf{r}),\mathbf{f}_m>\right]^{pq} = -\int_{T^p}\int_{T^q}\mathbf{f}_m\cdot\mathbf{M}\times\nabla G\,dS'dS$$
$$= \eta\int_{T^p}\int_{T^q}\hat{\mathbf{n}}'[\mathbf{f}_m\cdot(\underline{\mathbf{Z}}_s\cdot\mathbf{J})]\cdot\nabla G\,dS'dS \qquad (22)$$
$$+\eta\int_{T^p}\int_{T^q}(\mathbf{f}_m\cdot\hat{\mathbf{n}}')(\underline{\mathbf{Z}}_s\cdot\mathbf{J})\cdot\nabla' G\,dS'dS$$

where the magnetic surface current $\mathbf{M}$ has been related to the electric surface current $\mathbf{J}$ through the IBC relationship, and where $\mathbf{f}_m$ is the portion of the mth testing function within face p. The result in (22) has been expressed in a form in which the terms representing field components normal and tangential to the plane of the source are easily separated.

We consider first the field component tangential to the plane of the source triangle. For this component the contribution to a matrix element for the portion of the testing function $\mathbf{f}_i$ residing in face p and the basis function $\mathbf{f}_j$ in face q is

$$\eta\int_{T^p}\mathbf{f}_i^p\cdot\underline{\mathbf{Z}}_s\cdot\mathbf{I}_j^q\,dS = -\frac{\eta}{4\pi}\left(\frac{\ell_i\ell_j}{4A^pA^q}\right)\cdot$$
$$\left\{\int_{T^p}d\int_{T^q}(\mathbf{r}-\mathbf{r}_i)\cdot\underline{\mathbf{Z}}_s\cdot(\mathbf{r}'-\mathbf{r}_j)\,K(R)\,dS'dS\right. \qquad (23)$$
$$\left.+I_s\int_{T^p}(\mathbf{r}-\mathbf{r}_i)\cdot\underline{\mathbf{Z}}_s\cdot\mathbf{A}_j^q\,dS\right\}$$

with

$$K(R) = \frac{(1+jkR)e^{-jkR}-I_s(1+\tfrac{1}{2}k^2R^2)}{R^3}$$

where ℓ_n is the length of edge n, A^n is the area of face n, $d=\hat{\mathbf{n}}'\cdot\mathbf{R}$, $\mathbf{r}_n$ is the position vector to the triangle vertex opposite edge n, and where I_s is either one, if singularity extraction is to be performed, or zero, if not. The vector function $\mathbf{A}_j^q$ in (23) which results when singularity extraction is performed is defined by

$$\mathbf{A}_j^q = -d\mathbf{U}^q(\mathbf{r}) + (\rho-\rho_j)\frac{d}{|d|}V^q(\mathbf{r})$$
$$+\tfrac{1}{2}dk^2\mathbf{b}^q(\mathbf{r}) + \tfrac{1}{2}dk^2(\rho-\rho_j)a^q(\mathbf{r}) \qquad (24)$$

where $\mathbf{U}^q$, and V^q are defined as:

$$\mathbf{U}^q(\mathbf{r}) = \sum_j \hat{\mathbf{u}}_j \ln(G_j) \tag{25}$$

$$V^q(\mathbf{r}) = \sum_j \hat{\mathbf{P}}_j^0 \cdot \hat{\mathbf{u}}_j \left[\tan^{-1}(F_j^+) - \tan^{-1}(F_j^-)\right] \tag{26}$$

Other quantities appearing in (24) are defined in (15) through (18). The details of the evaluations leading to (24) through (26) are given in [29] and [30]. Evaluation of the electric vector potential integrals has been performed via a similar procedure in [28]. Another alternate procedure has been described in [31].

The source-region integration appearing on the right side in (23) is performed numerically. The term in (23) containing the source-region integration can be rewritten as

$$-\frac{\eta}{4\pi}\left[\frac{\ell_i \ell_j}{4A^p A^q}\right] \int_{T^p} \sum_{r=1}^{2}\sum_{s=1}^{2} [(\mathbf{r}-\mathbf{r}_i)\cdot\hat{\mathbf{a}}_r Z_{rs} \hat{\mathbf{a}}_s \cdot \mathbf{I}_{b_j}^q]\, dS \tag{27}$$

where

$$\mathbf{I}_{b_j}^q = \int_{T^q} (\mathbf{r}'-\mathbf{r}_j) d \left[\frac{(1+jkR)e^{-jkR} - I_s(1+\frac{1}{2}k^2R^2)}{R^3}\right] dS' \tag{28}$$

which has been previously evaluated numerically in the isotropic IBC case [29, 30]. The double dot product with the IBC dyadic in (23) has been represented as a double summation in (27). The portion of (23) resulting from analytical integration over the source region can be expressed similarly as

$$-I_s \frac{\eta}{4\pi}\left[\frac{\ell_i \ell_j}{4A^p A^q}\right] \int_{T^p} (\mathbf{r}-\mathbf{r}_i)\cdot \underline{\mathbf{Z}}_s \cdot \mathbf{A}_j^q\, dS \tag{29}$$

$$= -I_s \frac{\eta}{4\pi}\left[\frac{\ell_i \ell_j}{4A^p A^q}\right] \int_{T^p} \sum_{r=1}^{2}\sum_{s=1}^{2} Z_{rs}\, b_{i,r}^A\, b_{j,s}^B\, dS$$

where

$$b_{i,r}^A = (\mathbf{r}-\mathbf{r}_i)\cdot\hat{\mathbf{a}}_r \tag{30}$$

and

$$b_{j,s}^B = \hat{\mathbf{a}}_s \cdot \mathbf{A}_j^q(\mathbf{r}) \tag{31}$$

No new numerical or analytical integral evaluations are required for the field component tangential to the plane of the source in the anisotropic case. The terms obtained for the isotropic case are merely combined with different coefficients.

The component of the scattered electric field normal to the plane of the source triangle and arising from the magnetic current contribution in (22) is

$$\eta \int_{T^p} (\mathbf{f}_i^p \cdot \hat{\mathbf{n}}') \int_{T^q} (\underline{\mathbf{Z}}_s \cdot \mathbf{f}_j^q) \cdot \nabla' G\, dS' dS \tag{32}$$

The dyadic notation in (32) can be rewritten using the double summation as

$$\frac{\eta}{4\pi}\left[\frac{\ell_i \ell_j}{4A^p A^q}\right] \int_{T^p} [(\mathbf{r}-\mathbf{r}_i)\cdot\hat{\mathbf{n}}'] \int_{T^q} [\underline{\mathbf{Z}}_s \cdot (\mathbf{r}'-\mathbf{r}_j)] \cdot \nabla' G\, dS' dS$$

$$= -\frac{\eta}{4\pi}\left[\frac{\ell_i \ell_j}{4A^p A^q}\right] \int_{T^p} N_i(\mathbf{r}) \sum_{r=1}^{2}\sum_{s=1}^{2} [Z_{rs}\hat{\mathbf{a}}_r \cdot \mathbf{I}_{sj}(\mathbf{r})]\, dS \tag{33}$$

where $N_i(\mathbf{r}) = (\mathbf{r}-\mathbf{r}_i)\cdot\hat{\mathbf{n}}'$ and

$$\mathbf{I}_{sj}(\mathbf{r}) = -\int_{T^q} [\hat{\mathbf{a}}_s \cdot (\mathbf{r}'-\mathbf{r}_j)] \nabla' G\, dS' \tag{34}$$

The integral for $\mathbf{I}_{sj}(\mathbf{r})$ can be expressed in a more convenient form for implementation by using the identity $a\nabla b = \nabla(ab) - b\nabla a$ and the fact that $\hat{\mathbf{a}}_r$ is tangential to the source plane. One then obtains

$$\mathbf{I}_{sj}(\mathbf{r}) = -\int_{T^q} \nabla_s' \{[\hat{\mathbf{a}}_s \cdot (\mathbf{r}'-\mathbf{r}_j)] G\}\, dS' + \int_{T^q} G\, \nabla_s' [\hat{\mathbf{a}}_s \cdot (\mathbf{r}'-\mathbf{r}_j)]\, dS'$$

$$= -\int_{\partial T^q} [\hat{\mathbf{a}}_s \cdot (\mathbf{r}'-\mathbf{r}_j)] G\, \hat{\mathbf{u}}\, d\ell' + \int_{T^q} G\, \mathbf{H}_{sj}\, dS'$$

$$= -\mathbf{I}_{sj}^L + \mathbf{I}_{sj}^A \tag{35}$$

where $\hat{\mathbf{u}}$ is the outward-directed unit normal to the triangle boundary lying in the plane of the triangle and $\mathbf{H}_{sj}$ is a constant vector obtained by evaluating the gradient operation in the second term of (35):

$$\mathbf{H}_{sj} = \nabla_s' \{\hat{\mathbf{a}}_s \cdot [\xi_{j+1}(\mathbf{r}_{j+1}-\mathbf{r}_j) + \xi_{j-1}(\mathbf{r}_{j-1}-\mathbf{r}_j)]\}$$

$$= \hat{\mathbf{a}}_s \cdot \boldsymbol{\ell}_{j-1}\left[\frac{-\hat{\mathbf{h}}_{j+1}}{h_{j+1}}\right] - \hat{\mathbf{a}}_s \cdot \boldsymbol{\ell}_{j+1}\left[\frac{-\hat{\mathbf{h}}_{j-1}}{h_{j-1}}\right]$$

$$= -\frac{1}{2A^q}[(\hat{\mathbf{a}}_s \cdot \boldsymbol{\ell}_{j-1})(\boldsymbol{\ell}_{j+1} \times \hat{\mathbf{n}}') - (\hat{\mathbf{a}}_s \cdot \boldsymbol{\ell}_{j+1})(\boldsymbol{\ell}_{j-1} \times \hat{\mathbf{n}}')] \tag{36}$$

This result is obtained by expressing the vector basis

function variation $(\mathbf{r}'-\mathbf{r}_j)$ in area coordinates [28], as indicated in the first line of (36), where ξ_j is the area coordinate having value one at the vertex $\mathbf{r}_j$ and value zero at the vertices $\mathbf{r}_{j+1}$ and $\mathbf{r}_{j-1}$. The gradient operation on the jth area coordinate variable is then conveniently expressed in terms of the height of the jth vertex, h_j, and a vector directed normal to the jth edge, $\hat{\mathbf{h}}_j$ $(=\hat{\mathbf{u}}_j)$. Thus, $\mathbf{I}_{sj}(\mathbf{r})$ can be expressed as

$$\mathbf{I}_{sj}(\mathbf{r}) = \mathbf{H}_{sj}\int_{T^q} G^b\, dS' + \mathbf{H}_{sj}\int_{T^q} G^u\, dS'$$

$$-\int_{\partial T^q}[\hat{\mathbf{a}}_s\cdot(\mathbf{r}'-\mathbf{r}_j)]G^b\,\hat{\mathbf{u}}\,d\ell' - \int_{\partial T^q}[\hat{\mathbf{a}}_s\cdot(\mathbf{r}'-\mathbf{r}_j)]G^u\,\hat{\mathbf{u}}\,d\ell'$$

$$= \mathbf{H}_{sj}I_q^{Ab} + \mathbf{H}_{sj}I_q^{Au} - \mathbf{I}_{sj}^{Lb} - \mathbf{I}_{sj}^{Lu} \tag{37}$$

In (37) the superscript b indicates a term which is bounded or has a bounded integrand (when I_s is appropriately chosen), while the superscript u indicates a term which may be unbounded or may have an unbounded integrand. The superscript L indicates a line integral term, while the superscript A indicates an area integral term. The bounded and unbounded kernel terms are given by

$$G^b = \frac{e^{-jkR}-I_s}{R} \tag{38}$$

and

$$G^u = \frac{I_s}{R} \tag{39}$$

Thus, the terms involving the field component normal to the plane of the source triangle can be expressed as

$$-\frac{\eta}{4\pi}\left(\frac{\ell_i\ell_j}{4A^pA^q}\right)\left\{\sum_{r=1}^{2}\sum_{s=1}^{2}[Z_{rs}\mathbf{H}_{sj}\cdot\hat{\mathbf{a}}_r]\int_{T^p}N_i(\mathbf{r})[I_q^{Ab}+I_q^{Au}]\,dS\right.$$

$$\left.-\sum_{r=1}^{2}\sum_{s=1}^{2}Z_{rs}\int_{T^p}N_i(\mathbf{r})\hat{\mathbf{a}}_r\cdot[\mathbf{I}_{sj}^{Lb}(\mathbf{r})+\mathbf{I}_{sj}^{Lu}(\mathbf{r})]\,dS\right\} \tag{40}$$

where the area integrations over the source region are defined by

$$I_q^{Ab}(\mathbf{r}) = \int_{T^q}\frac{e^{-jkR}-I_s}{R}\,dS' \tag{41}$$

and

$$I_q^{Au}(\mathbf{r}) = a^q(\mathbf{r}) \tag{42}$$

while the line integrations around the source triangle are given by

$$\mathbf{I}_{sj}^{Lb}(\mathbf{r}) = [\hat{\mathbf{a}}_s\cdot\boldsymbol{\ell}_{j-1}]\sum_{k=j-1}^{j+1}\hat{\mathbf{u}}_k\int_{\partial_k T^q}\xi_{j+1}G^b\,d\ell'$$

$$-[\hat{\mathbf{a}}_s\cdot\boldsymbol{\ell}_{j+1}]\sum_{k=j-1}^{j+1}\hat{\mathbf{u}}_k\int_{\partial_k T^q}\xi_{j-1}G^b\,d\ell' \tag{43}$$

and

$$\mathbf{I}_{sj}^{Lu}(\mathbf{r}) = I_s[\hat{\mathbf{a}}_s\cdot\boldsymbol{\ell}_{j-1}]\sum_{k=j-1}^{j+1}\hat{\mathbf{u}}_k\int_{\partial_k T^q}\frac{\xi_{j+1}}{R}\,d\ell'$$

$$-I_s[\hat{\mathbf{a}}_s\cdot\boldsymbol{\ell}_{j+1}]\sum_{k=j-1}^{j+1}\hat{\mathbf{u}}_k\int_{\partial_k T^q}\frac{\xi_{j-1}}{R}\,d\ell' \tag{44}$$

The area integration terms given in (41) and (42) were evaluated in the isotropic case and are again simply combined with different coefficients in the anisotropic case. The line integrations indicated in (43) and (44), however, did not appear in the same form in the isotropic case. Therefore, new numerical and analytical line integral evaluations are required for the anisotropic IBC case. The new analytical integral evaluations required are indicated in (45) below.

$$\int_{\partial_i T^q}\frac{\xi_i}{R}\,d\ell' = 0$$

$$\int_{\partial_{i+1} T^q}\frac{\xi_i}{R}\,d\ell' = \frac{1}{\ell_{i+1}}[R_{i+1}^{+}-R_{i+1}^{-}-\ell_{i+1}^{-}\ell n(G_{i+1})] \tag{45}$$

$$\int_{\partial_{i-1} T^q}\frac{\xi_i}{R}\,d\ell' = -\frac{1}{\ell_{i-1}}[R_{i-1}^{+}-R_{i-1}^{-}-\ell_{i-1}^{+}\ell n(G_{i-1})]$$

The line integral term in (40) that may have an unbounded integrand can then be succinctly expressed as

$$\mathbf{I}_{sj}^{Lu}(\mathbf{r}) = I_s[\hat{\mathbf{a}}_s\cdot\boldsymbol{\ell}_{j-1}]\sum_{k=j-1}^{j+1}\hat{\mathbf{u}}_k L_k^{j+1}$$

$$-I_s[\hat{\mathbf{a}}_s\cdot\boldsymbol{\ell}_{j+1}]\sum_{k=j-1}^{j+1}\hat{\mathbf{u}}_k L_k^{j-1} \tag{46}$$

where

$$L_k^{\alpha} = \begin{cases} -\dfrac{1}{\ell_k}[R_k^{+}-R_k^{-}-\ell_k^{+}\ell n(G_k)] & , \quad k=\alpha-1 \\ \dfrac{1}{\ell_k}[R_k^{+}-R_k^{-}-\ell_k^{-}\ell n(G_k)] & , \quad k=\alpha+1 \\ 0 & , \quad k=\alpha \end{cases} \tag{47}$$

The special case in which the source and observation triangles are the same must also be reevaluated for the anisotropic case. The self term for the anisotropic case may be written as

$$\begin{aligned} <\mathbf{f}_i^q, \tfrac{1}{2}\hat{\mathbf{n}}\times\mathbf{M}_j^q> &= \tfrac{1}{2}\eta <\mathbf{f}_i^q, \underline{\mathbf{Z}}_s \cdot \mathbf{f}_j^q> \\ &= \frac{\ell_i \ell_j}{8(A^q)^2} \int_{T^q} (\rho' - \rho_i) \cdot \underline{\mathbf{Z}}_s \cdot (\rho' - \rho_j) dS' \end{aligned} \tag{48}$$

If the vector variation of the basis functions is expressed in terms of the area coordinates and the dyadic dot products are given in double summation form, the self term becomes

$$\begin{aligned} &\frac{\ell_i \ell_j}{8(A^q)^2} \int_{T^q} \sum_{r=1}^{2} \sum_{s=1}^{2} Z_{rs} \{[\xi_{i+1}(\mathbf{r}_{i+1} - \mathbf{r}_i) + \xi_{i-1}(\mathbf{r}_{i-1} - \mathbf{r}_i)] \cdot \hat{\mathbf{a}}_r\} \\ &\qquad \cdot \{\hat{\mathbf{a}}_s \cdot [\xi_{j+1}(\mathbf{r}_{j+1} - \mathbf{r}_j) + \xi_{j-1}(\mathbf{r}_{j-1} - \mathbf{r}_j)]\} \end{aligned}$$

$$\begin{aligned} = \frac{\ell_i \ell_j}{4(A^q)} \sum_{r=1}^{2} \sum_{s=1}^{2} Z_{rs} [&\alpha_{i-1,r} \alpha_{j-1,s} I_{i+1,j+1} \\ &- \alpha_{i-1,r} \alpha_{j+1,s} I_{i+1,j-1} \\ &- \alpha_{i+1,r} \alpha_{j-1,s} I_{i-1,j+1} \\ &+ \alpha_{i+1,r} \alpha_{j+1,s} I_{i-1,j-1}] \end{aligned} \tag{49}$$

where

$$\alpha_{mn} = \ell_m \cdot \hat{\mathbf{a}}_n \tag{50}$$

and

$$I_{mn} = \int_{\xi_1=0}^{1} \int_{\xi_2=0}^{1-\xi_1} \xi_m \xi_n \, d\xi_2 \, d\xi_1 = \begin{cases} \dfrac{1}{12}, & m = n \\ \dfrac{1}{24}, & m \neq n \end{cases} \tag{51}$$

The preceding expressions have been implemented in the evaluation of the impedance matrix for the triangular patch scattering code. The resulting system of linear equations is solved in the usual manner for the surface current distribution. Once the surface current distribution on the scatterer has been computed, the far scattered electric field may be determined from

$$\mathbf{E}^s \simeq -C(r)\eta \int_S G_f \, [\mathbf{J} - \hat{\mathbf{r}}(\mathbf{J} \cdot \hat{\mathbf{r}})] dS' + C(r) \int_S G_f \, (\hat{\mathbf{r}} \times \mathbf{M}) dS' \tag{52}$$

where

$$C(r) = \frac{jk}{4\pi r} e^{-jkr} \tag{53}$$

and

$$G_f = e^{jk(\hat{\mathbf{r}} \cdot \mathbf{r}')} \tag{54}$$

After substitution of the IBC relating the electric and magnetic current, the θ and ϕ components of the far scattered electric field can be represented as

$$E_\theta = -\eta C(r) \int_S G_f \, \mathbf{J} \cdot \{\hat{\theta} - \sum_{r=1}^{2} \sum_{s=1}^{2} [(\hat{\phi} \times \hat{\mathbf{n}}') \cdot \hat{\mathbf{a}}_r] Z_{rs} \hat{\mathbf{a}}_s\} \, dS' \tag{55}$$

and

$$E_\phi = -\eta C(r) \int_S G_f \, \mathbf{J} \cdot \{\hat{\phi} + \sum_{r=1}^{2} \sum_{s=1}^{2} [(\hat{\theta} \times \hat{\mathbf{n}}') \cdot \hat{\mathbf{a}}_r] Z_{rs} \hat{\mathbf{a}}_s\} \, dS' \tag{56}$$

The far scattered electric field may then be represented conveniently in terms of pattern integrals P_θ and P_ϕ as

$$\mathbf{E}^s = -\eta C(r)[P_\theta \hat{\theta} + P_\phi \hat{\phi}] \tag{57}$$

where the pattern integral due to a single source face q is given by

$$\begin{aligned} P_\alpha^q = \sum_{i=1}^{3} s_i \frac{I_i \ell_i}{2A^q} \int_{T^q} G_f \, (\mathbf{r}' - \mathbf{r}_i) \cdot \{\hat{\alpha} \\ + \sum_{r=1}^{2} \sum_{s=1}^{2} [(\hat{\alpha} \times \hat{\mathbf{r}}) \times \hat{\mathbf{n}}'] \cdot \hat{\mathbf{a}}_r Z_{rs} \hat{\mathbf{a}}_s\} \, dS' \end{aligned} \tag{58}$$

with α replaced by either θ or ϕ. In (58), $s_i = \pm 1$, the plus sign being chosen if the basis function for edge i is directed away from vertex i in face q, and the minus sign being chosen if the basis function is directed toward the vertex. The integration over the source region in (58) can be performed analytically to obtain

$$\begin{aligned} P_\alpha^q &\approx \sum_{i=1}^{3} s_i \frac{I_i \ell_i}{2A^q} e^{jk(\hat{\mathbf{r}} \cdot \mathbf{r}^{cq})} \boldsymbol{\gamma} \cdot \int_{T^q} (\mathbf{r}' - \mathbf{r}_i) \, dS' \\ &= \tfrac{1}{2} \sum_{i=1}^{3} s_i I_i \ell_i e^{jk(\hat{\mathbf{r}} \cdot \mathbf{r}^{cq})} \boldsymbol{\gamma} \cdot (\mathbf{r}^{cq} - \mathbf{r}_i) \end{aligned} \tag{59}$$

where

$$\boldsymbol{\gamma} = \hat{\alpha} + \sum_{r=1}^{2} \sum_{s=1}^{2} [(\hat{\alpha} \times \hat{\mathbf{r}}) \times \hat{\mathbf{n}}'] \cdot \hat{\mathbf{a}}_r] Z_{rs} \hat{\mathbf{a}}_s \tag{60}$$

Thus, the final result may also be expressed as

$$P_\alpha^q = \tfrac{1}{2}\sum_{i=1}^{3} s_i I_i \ell_i e^{jk(\hat{\mathbf{r}}\cdot\mathbf{r}^{cq})}[\hat{\boldsymbol{\alpha}}\cdot(\mathbf{r}^{cq}-\mathbf{r}_i) + (\hat{\boldsymbol{\alpha}}\times\hat{\mathbf{r}})\cdot\sum_{r=1}^{2}\sum_{s=1}^{2}(\hat{\mathbf{n}}'\times\hat{\mathbf{a}}_r)Z_{rs}\hat{\mathbf{a}}_s\cdot(\mathbf{r}^{cq}-\mathbf{r}_i)] \quad (61)$$

IV. Numerical Results

The procedures described in the previous section were initially implemented into a modified version of the original triangular patch code [22] and were subsequently incorporated into the more sophisticated IBC3D scattering code [30]. Numerical results are presented here for several spherical and cylindrical geometries with isotropic or anisotropic surface impedance boundary conditions. Results obtained using the triangular patch code and body of revolution codes are compared.

We first consider a cylindrical scatterer geometry with geometrical parameters as shown in Fig. 3. The cylinder is assumed to have length L and radius a. A standard

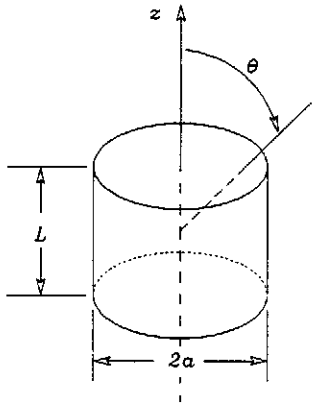

Figure 3. Geometrical parameters for cylinder.

cylindrical coordinate system is used for the body of revolution model with the z axis being the axis of revolution. For the triangular patch code, the axis of the cylinder was oriented along the y axis. Data obtained in the rotated coordinate system of the patch code model, however, are presented relative to the coordinate system of Fig. 3 in each case.

The first example considered is that of a small cylinder with length $L=0.2\lambda$ and radius $a=0.1\lambda$. The triangular patch model used to obtain the results presented is shown in Fig. 4. This triangular patch model uses 16 linear segments to model the geometry in the azimuthal direction, 4 segments along the cylinder radius, and 6 segments along the cylinder length. The quadrilateral patches formed by the azimuthal and generating contour segmentations are then divided by a line segment to form the triangular patches. The resulting patch model has 624 unknowns. The monostatic radar cross section results obtained with the triangular patch code and a body of revolution code modified to solve the anisotropic IBC problem [20] are shown in Fig. 5. For this case a θ-polarized plane wave is the excitation and the anisotropic surface impedance is defined by $\underline{\mathbf{Z}}_s = \hat{\mathbf{t}}\hat{\boldsymbol{\phi}}$, corresponding to a single non-zero, off-diagonal element in the impedance dyadic (6). Results are shown for the co-polarized and cross-polarized components of the radar cross section. The agreement between the results obtained by the two different methods is excellent.

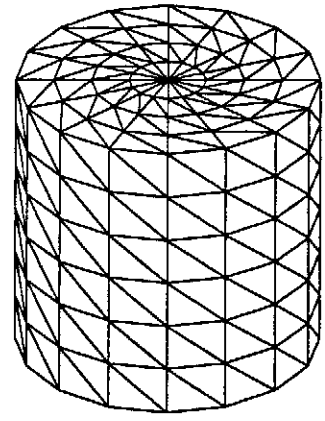

Figure 4. Triangular patch model for a cylinder of length $L=0.2\lambda$ and radius $a=0.1\lambda$.

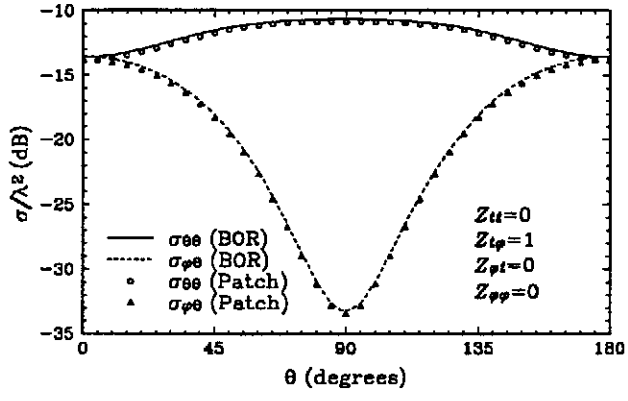

Figure 5. Comparison of monostatic radar cross section results for a small cylinder with an anisotropic impedance boundary condition.

Results were also obtained for a larger, resonant length

cylinder of length $L=\lambda$ and radius $a=0.1\lambda$. One triangular patch model used for this cylinder is shown in Fig. 6. A second model with more unknowns is shown in Fig. 7. The model of Fig. 6 has 220 triangular faces and 330 unknowns. The model is generated using 10 linear segments to model the surface in the azimuthal direction, 2 segments in the radial direction, and 8 segments along the length of the

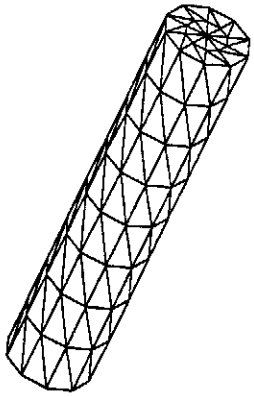

Figure 6. Triangular patch model of a cylinder with 330 unknowns ($L=\lambda$, $a=0.1\lambda$).

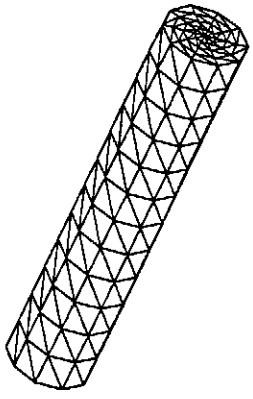

Figure 7. Triangular patch model of a cylinder with 570 unknowns ($L=\lambda$, $a=0.1\lambda$).

cylinder. The model of Fig. 7 has 570 unknowns. It is generated using 10 linear segments to model the surface in the azimuthal direction again, but with 4 segments in the radial direction and 12 segments along the length of the cylinder. Results obtained for the triangular patch model of Fig. 6 are compared with those obtained from the modified body of revolution formulation in Figs. 8 and 9 for the co-polarized and cross polarized radar cross section components, respectively. For the body of revolution model, the generating contour was modeled by 32 linear segments, resulting in 126 unknowns. The anisotropic surface impedance is again defined by $\underline{Z}_s = \hat{t}\hat{\phi}$. The agreement of the results is generally very good except for near-axial incidence and, for $\sigma_{\phi\theta}$, in the case of broadside incidence. The disagreement between the data obtained by the two different methods for axial incidence is believed to indicate slow convergence (for both approaches) due to discretization error. It seems likely that the error at broadside incidence is partially due to insufficient resolution of the triangular patch model in the azimuthal direction.

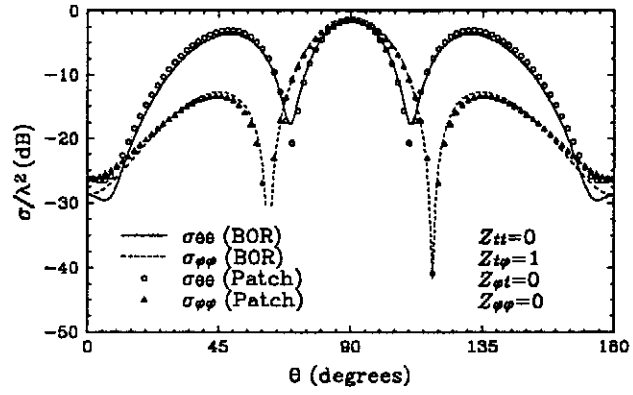

Figure 8. Comparison of co-polarized monostatic radar cross section results obtained with body of revolution and triangular patch models.

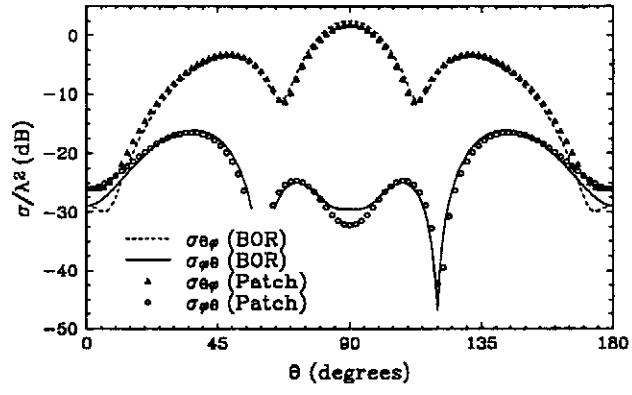

Figure 9. Comparison of cross-polarized monostatic radar cross section results obtained with body of revolution and triangular patch models.

For the triangular patch model of Fig. 7, the results are compared with those obtained from the modified body of revolution formulation in Figs. 10 and 11 for the co-polarized and cross-polarized radar cross section components, respectively. The generating contour for the body of revolution model in this case was defined by 56 linear segments, resulting in 222 unknowns. The agreement

between the results obtained by the two different methods is generally very good, and it is clear that the increased number of unknowns in both methods has improved the agreement between the two methods for axial and broadside illumination.

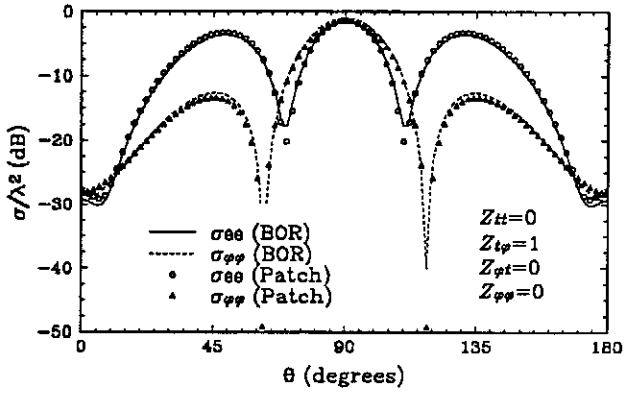

Figure 10. Comparison of co-polarized radar cross section results obtained with body of revolution and triangular patch models.

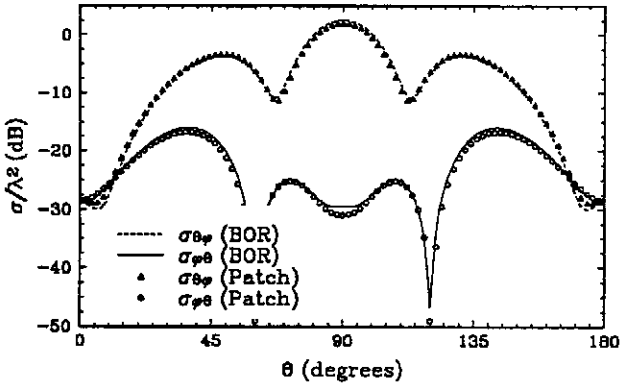

Figure 11. Comparison of cross-polarized radar cross section results obtained with body of revolution and triangular patch models.

We next consider the case of a sphere, both with an isotropic IBC and with an anisotropic IBC. In both cases, the results obtained using the IBC3D patch code are compared with an independent IBC body of revolution code (JRMBOR [32]). Comparisons are also made with the predictions of Weston's theorem [33] for the anisotropic IBC case. Three different triangular patch models, with 260, 570, and 1616 unknowns, were used to represent the sphere for the isotropic IBC case. The two models with the larger number of unknowns are shown in Fig. 12. Calculated backscatter cross-sections, normalized by πa^2, where a is the sphere radius, are shown in Fig. 13 for the isotropic IBC case (i.e., in (6) $Z_{11}=Z_{22}=0.1+j0.1$, and $Z_{12}=Z_{21}=0$) as a function of $ka=2\pi a/\lambda$, where λ is the excitation wavelength. For $ka=3$, the segmentations of the three IBC3D models correspond to about 7, 11, and 18 triangles per wavelength. The JRMBOR result used at least 25 triangles per wavelength, and consequently, was reasonably well converged. The plotted IBC3D results have been radius-corrected to account for the difference in surface area of the inscribed triangle model of the sphere and the actual sphere. The radius correction factors for the 260, 570, and 1616 patch models were 0.988, 0.991, and 0.998, respectively. The IBC3D results are observed to converge to the JRMBOR solution as the triangle segmentation is increased. For the 1616, patch model, the agreement is nearly precise for $ka=2$, with differences no greater than a small fraction of a dB for $ka=3$.

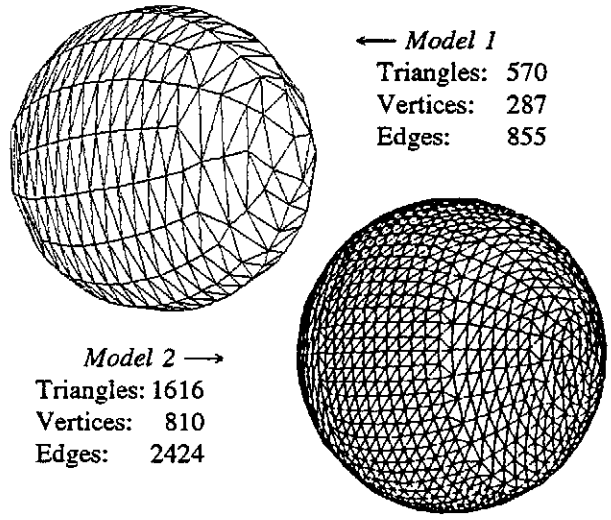

Figure 12. Triangulated sphere models.

Note that the 260 triangle patch model has spikes at $ka\approx2.75$ and $ka\approx3.9$. The spikes are an artifact of the EFIE formulation used, and they appear at the internal resonance frequencies of a perfect electric conductor (PEC) scatterer having the same surface. The width of the spike decreases as the number of patches increases, and, due to the finite sampling in frequency, the 570 triangle model shows only a small kink near $ka\approx3.9$. The JRMBOR code result was obtained with a combined field integral equation (CFIE) formulation using equal weightings of the EFIE and MFIE, which tends to suppress the spurious internal resonances [34].

IBC3D results and the JRMBOR results have also been compared for the case of a sphere with an anisotropic IBC

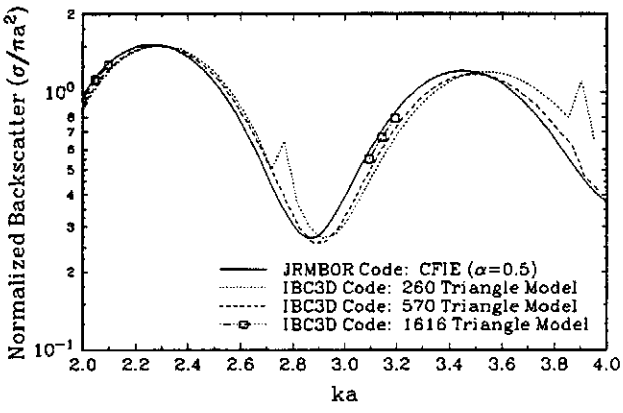

Figure 13. Comparison of IBC3D and JRMBOR for an isotropic impedance sphere ($Z_s=0.1+j0.1$).

and size $ka=1$ in Fig. 14. The geometry is shown in the figure, where the dashed line represents an axis of symmetry of the body, and $\hat{k}$ is a unit vector in the direction of propagation of the incident plane wave. The plane of scattering is defined by these two lines, and the angle θ between them is the scattering angle plotted in Fig. 14. Vertical polarization (V) corresponds to the case where the electric field is perpendicular to the plane of scattering, while horizontal polarization (H) has the electric field in the plane of scattering. The intersection section of the axis of symmetry (dashed line) with the surface of the sphere defines one pole of the sphere. The unit vectors $\hat{a}_1$ in (6) are chosen to be everywhere tangential to the surface of the sphere and directed toward the pole, while the unit vectors $\hat{a}_2$ are in the azimuthal direction on the sphere surface. The surface impedance for the case is then defined as

$$\underline{Z}_s = \begin{bmatrix} 4.0 & 0 \\ 0 & 0.25 \end{bmatrix}$$

Results for the PEC sphere case are also shown (dashed curve) in Fig. 14, and the IBC3D and JRMBOR results are virtually indistinguishable. For the anisotropic IBC case, the surface impedance is defined so that the product of the diagonal matrix elements is unity. As a consequence, a generalization of Weston's theorem [33] to anisotropic BORs [35] is applicable, and the backscatter RCS along the axis of symmetry should vanish. It can be seen in Fig. 14 that the RCS along the axis of symmetry ($\theta=0°$, 180°) is 45 dB lower than the PEC case. Also shown is the comparison between JRMBOR and IBC3D results (dotted and solid lines, respectively). The agreement between the two codes is quite good except for the smallest cross-section regions of the curve, where increased model segmentation is required to obtain more precise agreement. The generalized Weston theorem also requires that the VV and HH polarization results should be the same [35]. Both sets of numerically computed results exhibit this behavior except over the region of the curve where the cross section is small. The JRMBOR results were obtained using a segmentation equivalent to 40 triangles per wavelength, while the IBC3D results were obtained using about 27 triangles per wavelength.

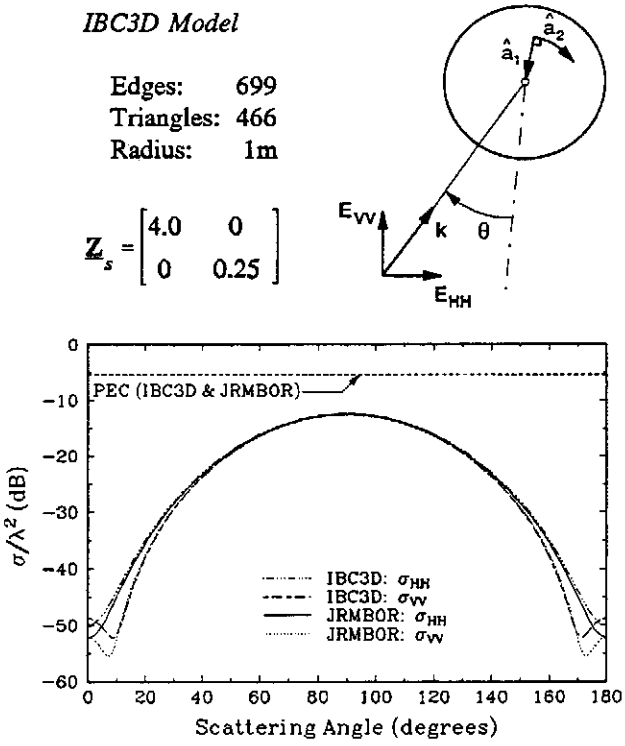

Figure 14. Comparison of IBC3D and JRMBOR bistatic scattering cross section for an anisotropic impedance sphere.

As a final example, we consider the case of another cylinder with an anisotropic IBC. The cylinder model is the same as that shown in Fig. 6, with length $L=\lambda$ and radius $a=0.1\lambda$. The unit vectors $\hat{a}_1$ and $\hat{a}_2$ that define the dyadic surface impedance are chosen to correspond to the azimuthal unit vector $\hat{\phi}$ and the generating arc unit vector $\hat{t}$ commonly used in BOR representations. Thus, $\hat{a}_1$ is on the cylinder surface and azimuthally directed with respect to the axis of symmetry of the cylinder. Along the length of the cylinder, the vector $\hat{a}_2$ is parallel to the axis of symmetry, but on the endcaps, $\hat{a}_2$ is radially directed. The cylinder has roughly 8.5 triangles per wavelength. The JRMBOR results were obtained using the CFIE formulation

with equal weight to the EFIE and MFIE. Fourier modes zero through five and a Gaussian quadrature order of 30 were used. There were about 25 triangles per wavelength for the JRMBOR model. Thus, one might expect the JRMBOR calculations to be more accurate than those of IBC3D for this case.

Fig. 15 shows the comparison between the predictions of IBC3D and JRMBOR when the cylinder has an anisotropic surface IBC with unequal diagonal elements. The plane of scattering and the horizontal and vertical polarizations are defined in the same manner as in the preceding case of the sphere. The HH results shown in Fig. 15 for a horizontally polarized transmitter and receiver are almost coincident, while there is a worst-case discrepancy of less than 2 dB for the VV polarization result at about 45°. This agreement seems quite reasonable considering the rather crude segmentation of the IBC3D patch model.

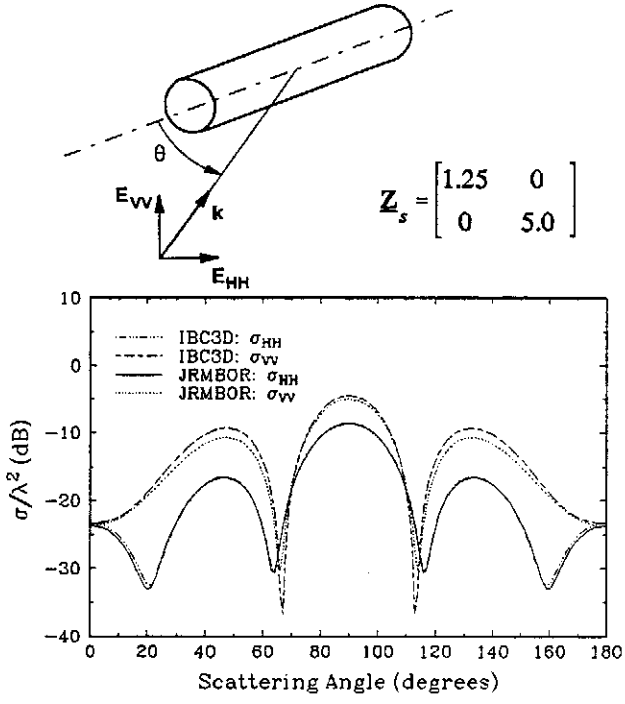

Figure 15. Comparison of IBC3D and JRMBOR monostatic RCS results for a cylinder with an anisotropic impedance boundary condition.

V. Summary

In this work the problem of electromagnetic scattering from arbitrarily shaped, imperfectly conducting surfaces modeled by an anisotropic impedance boundary condition has been considered. The numerical solution has been implemented using the electric field integral equation and a triangular patch model for the scatterer surface. The anisotropic impedance boundary condition function has been specified by a constant surface dyadic within each triangular face. Good agreement between numerical results obtained with the triangular patch model and a body of revolution model has been observed for the scattering cross sections of spheres and cylinders for both isotropic and anisotropic impedance boundary conditions.

References

[1] M. A. Leontovich, "Approximate boundary conditions for the electromagnetic field on the surface of a good conductor," *Investigations on Radiowave Propagation, Part II*, pp. 5-12, Printing House of the Academy of Sciences, Moscow, 1948.

[2] T. B. A. Senior, "Impedance boundary conditions for imperfectly conducting surfaces," *Appl. Sci. Res.*, Sect. B, no. 8, pp. 418-436, 1960.

[3] K. M. Mitzner, "An integral equation approach to scattering from a body of finite conductivity," *Radio Sci.*, vol. 2, no. 12, pp. 1459-1470, 1967.

[4] R. D. Graglia and P. L. E. Uslenghi, "Surface currents on impedance bodies of revolution," *IEEE Trans. Antennas Propagat.*, vol. AP-36, no. 9, pp. 1313-1317, September 1988.

[5] P. L. Huddleston, "Scattering by finite, open cylinders using approximate boundary conditions," *IEEE Trans. Antennas Propagat.*, vol. AP-37, no. 2, pp. 253-256, February 1989.

[6] K. A. Iskander, L. Shafai, A. Fransen, and J. E. Hansen, "Application of impedance boundary conditions to numerical solution of corrugated circular horns," *IEEE Trans. Antennas Propagat.*, vol. AP-30, no. 3, pp. 366-372, May 1982.

[7] T. B. A. Senior, "Impedance boundary conditions for statistically rough surfaces," *Appl. Sci. Res.*, Sect. B, no. 8, pp. 437-462, 1960.

[8] J. R. Wait and C. M. Jackson, "Calculations of the bistatic scattering cross section of a sphere with an impedance boundary condition," *Radio Sci. J. Res. Nat. Bur. Stand./USNC-URSI*, vol. 69D, no. 2, pp. 299-315, 1965.

[9] G. E. Heath, "Impedance boundary condition integral equations," *IEEE AP-S International Symposium Digest, Vol. II*, pp. 697-700, IEEE, Piscataway, 1984.

[10] A. A. Kishk, "Electromagnetic scattering from composite objects using a mixture of exact and impedance boundary conditions," *IEEE Trans. Antennas Propagat.*, vol. AP-39, no. 6, pp. 826-833, June1991.

[11] L. N. Medgyesi-Mitschang and J. M. Putnam,

"Integral equation formulations for imperfectly conducting scatterers," *IEEE Trans. Antennas Propagat.*, vol. AP-33, no. 2, pp. 206-214, February 1985.

[12] J. R. Rogers, "On combined source solutions for bodies with impedance boundary conditions, "*IEEE Trans. Antennas Propagat.*, vol. AP-33, no. 4, pp. 462-464, April 1985.

[13] W. V. T. Rusch and R. J. Pogorzelski, "A mixed-field solution for scattering from composite bodies," *IEEE Trans. Antennas Propagat.*, vol. AP-34, no. 7, pp. 955-958, July 1986.

[14] A. Sebak and L. Shafai, "Performance of various integral equation formulations for numerical solution of scattering by impedance objects," *Can. J. Phys.*, vol. 62, pp. 605-615, 1984.

[15] A. Sebak and L. Shafai, "Scattering from arbitrarily-shaped objects with impedance boundary conditions," *IEE Proc, Part H*, vol. 136, no. 5, pp. 371-376, 1989.

[16] A. W. Glisson, "Electromagnetic scattering by arbitrarily shaped surfaces with impedance boundary conditions," *Radio Science*, vol. 27, no. 6, pp. 935-943, 1992.

[17] T. B. A. Senior and J. L. Volakis, "Generalized impedance boundary conditions in scattering," *Proc. IEEE*, vol. 79, no. 10, pp. 1413-1420, October 1991.

[18] D. J. Hoppe and Y. Rahmat-Samii, "Higher order impedance boundary conditions applied to scattering by coated bodies of revolution," *IEEE Trans. Antennas Propagat.*, vol. AP-42, no. 12, pp. 1600-1611, December 1994.

[19] R. Orta, R. Tascone, G. Tessitore, and R. Zich, "Frequency selective surfaces made of anisotropic material (antennas)," *Proc. Int. Conf. Electromagnetics in Aerospace Applications*, Torino, Italy, pp. 341-345, 1989.

[20] A. W. Glisson, Mark Orman, Frank Falco, and Donald Koppel, "Electromagnetic scattering by a body of revolution with a general anisotropic impedance boundary condition," *IEEE AP-S International Symposium Digest, Vol. IV*, pp. 1997-2000, Chicago, IL, 1992.

[21] A. H. Chang, K. S. Yee, and J. Prodan, "Comparison of different integral equation formulations for bodies of revolution with anisotropic surface impedance boundary conditions," *IEEE Trans. Antennas Propagat.*, vol. AP-40, no. 8, pp. 989-991, August 1992.

[22] S. M. Rao, D. R. Wilton, and A. W. Glisson, "Electromagnetic scattering by surfaces of arbitrary shape," *IEEE Trans. Antennas Propagat.*, vol. AP-30, no. 3, pp. 409-418, May 1982.

[23] A. W. Glisson and M. Orman, "Implementation of the impedance boundary condition in the triangular-patch scattering code for thin scatterers," *IEEE AP-S International Symposium Digest, Vol. III*, pp. 1756-1759, London, Ontario, Canada, 1991.

[24] R. F. Harrington, *Time Harmonic Electromagnetic Fields*. New York: McGraw-Hill, 1961.

[25] R. F. Harrington, *Field Computation by Moment Methods*, 229 pp., Macmillan, New York, 1968.

[26] D. R. Wilton, S. M. Rao, A. W. Glisson, D. H. Schaubert, O. M. Al-Bundak, and C. M. Butler, "Potential integrals for uniform and linear source distributions on polygonal and polyhedral domains," *IEEE Trans. Antennas Propagat.*, vol. AP-32, no. 3, pp. 276-281, March 1984.

[27] J. Van Bladel, *Electromagnetic Fields*. New York: McGraw-Hill, 1964, p. 502.

[28] S. V. Yesantharao, *EMPACK–A software toolbox of potential integrals for computational electromagnetics*. M. S. Thesis, University of Houston, Houston, Texas, December 1989.

[29] A. W. Glisson, "Technical considerations for the implementation of the impedance boundary condition in the triangular-patch electromagnetic scattering code," Report No. FR-1, Subcontract No. C95-AWG, for Riverside Research Institute, New York, NY, December 1990.

[30] F. Falco, D. Koppel, N. Erlbach, and M. Orman, "Anisotropic impedance boundary condition 3D scattering code (IBC3D): Vol. I -- User's manual and programmer's guide," Technical Report, Riverside Research Institute, November 1991.

[31] R. D. Graglia, "On the numerical integration of the linear shape functions times the 3-D Green's function or its gradient on a plane triangle," *IEEE Trans. Antennas Propagat.*, vol. AP-41, no. 10, pp. 1448-1455, October 1993.

[32] J. R. Rogers, "JRMBOR - Program description and user's guide," Technical Report, Atlantic Aerospace Electronics Corporation, Greenbelt, Maryland, June 1989.

[33] V. H. Weston, "Theory of absorbers in scattering," *IEEE Trans. Antennas Propagat.*, vol. AP-11, no. 5, pp. 578-584, September 1963.

[34] J. R. Mautz and R. F. Harrington, "Electromagnetic scattering from a homogeneous material body of revolution," *Arch. Elek. Übertrag.*, vol. 33, no. 2, pp. 71-80, 1979.

[35] K. S. Yee and A. H. Chang, "Scattering theorems with anisotropic surface boundary conditions for bodies of revolution," *IEEE Trans. Antennas Propagat.*, vol. AP-39, no. 7, pp. 1041-1043, July 1991.